Adaptive Virtual Impedance-Based Fault Current Limiting Strategy for Grid-Forming Inverters

Fengshun JIAO, Jie ZHANG, Xinming JIANG, Xinyue LI, Yunyan YANG, and Tao XIE

***Abstract*—Grid-forming inverters (GFIs), which can mimic the behaviors of conventional synchronous generators to provide the frequency and voltage support for the electricity grids, face the challenge of overcurrent during grid faults due to the voltage-source output characteristics. The power semiconductors of inverters are incapable to withstand fault current and easily destroyed. To tackle the overcurrent dilemma encountered by GFIs during voltage drops, this paper proposes an adaptive virtual impedance-based fault current limiting strategy. This adaptive strategy can adjust dynamically the virtual impedance value in real-time based on the magnitude of fault currents, and thereby suppress fault currents effectively. To analyze the impacts of the adaptive impedance on the stability of GFIs, an impedance model composed of the adaptive impedance, grid and voltage control loops, is established in the *dq* reference frame. The influence of the adaptive virtual impedance control parameters on the stability of the grid-forming inverter system is evaluated through the generalized Nyquist criterion. The efficacy of the proposed adaptive virtual impedance strategy in fault current limitation and the accuracy of the stability analysis are validated through the comprehensive simulation results carried out in Matlab/Simulink and OPAL-RT semi-physical platform.**

***Index Terms*—Adaptive virtual impedance, fault current limitation, stability analysis, voltage-source inverter.**

I. Introduction

NOWADAYS, the modern power system has experienced a rapid evolution, leading to the gradual prominence of two key features, namely high proportion of renewable energy sources and high proportion of power electronics. Consequently, the traditional power grid, which was predominantly reliant on the synchronous generators, has undergone changes in its operational modes and characteristics across various time scales.

Manuscript received April 26, 2024; revised July 15, 2024; accepted August 12, 2024. Date of publication September 30, 2024; date of current version August 30, 2024. This work was supported by Shenzhen power supply Bureau scientific research project under Grant 090000202303010309013 28. *(Corresponding author: Xinyue Li.)*

F. Jiao, J. Zhang, X. Jiang, Y. Yang, and T. Xie are with the Shenzhen Power Supply Bureau of China Southern Power Grid, Shenzhen 518001, China (e-mails: 497940490@qq.com; 393289561@qq.com; terrynonstop@163.com; 13809884307@163.com; 974642857@qq.com).

X. Li is with the School of Mechanical Engineering and Automation, Harbin Institute of Technology (Shenzhen), Shenzhen 518055, China (e-mails: 530382583@qq.com).

Digital Object Identifier 10.24295/CPSSTPEA.2024.00015

The integration of high penetration of wind power, photovoltaics (PV), and electrochemical energy storage systems into the power grid through grid-connected inverters exhibits the characteristics of either the constant power or the constant current, resulting in a decrease in grid inertia, strength and poor disturbance immunity [1], [2]. To mimic the behaviors of traditional synchronous generators, a grid-forming control method has been adopted [3]. Unlike the conventional grid-following control method, the inverter is controlled as a voltage source under the grid-forming control method, enabling it to independently regular the system voltage and frequency, and achieve suppression of disturbances in the large power grid based on the emulated swing characteristics and excitation characteristics of synchronous generator.

Grid-forming inverters (GFIs) suffer from high short-circuit currents during grid faults, due to the voltage source characteristics. The conventional synchronous generators can bear the fault currents 5 to 7 times higher than their rated current, while GFIs can only temporarily sustain currents that are 1.2 to 2 times their rated current [4]. Moreover, excessive transient currents can trigger protective actions to disconnect in the inverters from the grid, degrading the stability of the system.

It is essential to limit the transient currents of GFIs during grid faults. Currently, the main strategies to limit the fault current include the current limiter [5], voltage limiter [6], and virtual impedance [7] methods. The current limiter method limits the fault current by introducing a saturator after the reference signal of the current loop. This method introduces the nonlinearity into the control loop, due to the direct restriction of the current reference. When the reference signal of the current loop reaches the clamping threshold, the system is controlled solely by the current loop, which results in the instable issues potentially. Additionally, the voltage loop is unable to control the voltage, resulting in the saturation of the voltage controller. After grid fault clearance, the system may fail to retain the stability [8]. The voltage limiter method limits the fault current by constraining the difference between the inverter terminal voltage and the point of common coupling (PCC) voltage, typically without using the voltage-current inner loop control [9]. This method requires a phase-locked loop to detect the PCC voltage amplitude and phase. During grid faults, the PCC voltage may fluctuate, leading to instability as well. The virtual impedance method limits the short-circuit current by subtracting the voltage drop across the virtual impedance from the reference voltage without introducing the nonlinearity. Furthermore, the adaptive virtual impedance method was

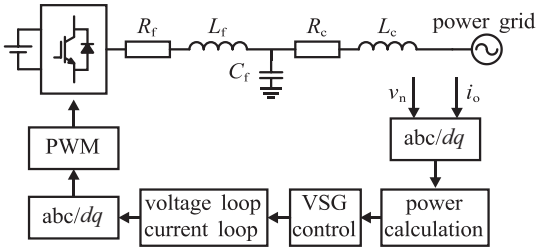

Fig. 1. Topology of a grid-connected inverter.

proposed and the virtual impedance was adaptively adjusted according to magnitude of current [10]. Compared with the approaches with current limiter and voltage limiter method, the adaptive virtual impedance method exhibits better ability to restore stability after fault recovery.

However, the current loop was not used in [10], degrading the power quality of GFM converters. To improve the power quality, this paper uses an adaptive virtual impedance strategy with a cascaded voltage and current inner loop. Furthermore, the sequence impedance was used to analyze the small signal stability in [10]. The sequence impedance introduces complex coefficient into transfer function, resulting in an asymmetry in the bode diagram. A *dq*-axis impedance model of the system is established in this paper, and the impact of virtual impedance parameters on system stability is analyzed using the generalized Nyquist criterion.

The rest of this paper is organized as follows: The control principle of grid-forming inverter is explained in Section II. The stability of the grid-forming inverter with adaptive virtual impedance is analyzed in Section III. The electromagnetic transient model is built to verify the stability and the rationality of the proposed control strategy in Section IV.

II. Control Principle of GFIs

The topology and control block diagram of a GFI are shown in Fig. 1, where the control strategy is composed of the virtual synchronous generator (VSG) control-based power loop, and voltage and current control loop. By adjusting the magnitude and phase of the inverter output voltage, the control scheme achieves power control, mimicking the behaviors of the synchronous generators. The VSG control loop includes the active power-frequency control and reactive power-voltage control, as depicted in Fig. 2.

When there is a grid voltage drop at the point of common coupling (PCC), the low impedance of the connecting lines leads to an increase of the inverter output current. This poses a risk of overcurrent damage to the power semiconductor devices within the inverter, thereby reducing the reliability of grid power supply. Hence, it is necessary to limit the fault current to mitigate the potential negative effects caused by fault current.

By introducing an output current feedforward into the voltage loop, a virtual impedance element is incorporated, which effectively reduces the voltage reference value of GFIs, thereby reducing the magnitude of fault current. After

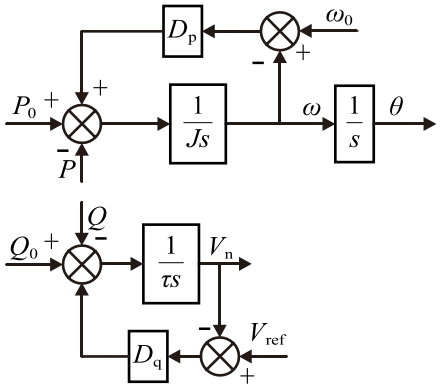

Fig. 2. Control block diagram of VSG control.

incorporating the virtual impedance, the voltage reference value calculation formula in the synchronous rotating reference frame can be represented as:

$$\begin{bmatrix} u_{d\text{ref}} \\ u_{q\text{ref}} \end{bmatrix} = \begin{bmatrix} e_d \\ e_q \end{bmatrix} - \left(\begin{bmatrix} R_v & 0 \\ 0 & R_v \end{bmatrix} + \begin{bmatrix} 0 & -X_v \\ X_v & 0 \end{bmatrix} \right) \begin{bmatrix} i_{od} \\ i_{oq} \end{bmatrix} \quad (1)$$

where the subscripts d and q represent the d-axis and q-axis components, respectively. i_o is the output current, e is the voltage output from the VSG loop and u_{ref} is voltage reference, R_v and X_v are the virtual resistance and reactance, respectively.

The block diagram of cascaded voltage and current control, incorporating the virtual impedance element as shown in (1), is presented in Fig. 3. In the diagram, v_g、v_n、ω_n and L_f represent the grid-side voltage, inverter output voltage, system angular frequency, and inverter-side filtering inductance, respectively. $G_v(s)$ and $G_c(s)$ represent the PI controllers for the voltage loop and current loop, respectively.

The fault current can be calculated as:

$$I = \frac{V_n - V_g}{R_v + j\omega_n \left(X_v + X_c \right)} \quad (2)$$

where V_n and V_g represent the inverter output voltage and the grid voltage, respectively, X_c denotes the reactance of the grid-side filtering inductance.

It can be seen from (2) that the virtual impedance can help to limit the fault current, but lacks the ability to adjust the virtual impedance appropriately based on the extent of voltage drop. As a result, it cannot effectively restrict the fault current. In light of this, this paper proposes an adaptive virtual impedance current limiting strategy to achieve better current suppression. The control block diagram for this strategy is explained in Fig. 4. In the diagram, I_{th} represents the current threshold, and I_{omag} denotes the magnitude of the grid current. The calculation formula for the grid current magnitude is as:

$$I_{\text{omag}} = \sqrt{i_{od}^2 + i_{od}^2} \quad (3)$$

When I_{omag} exceeds I_{th}, the adaptive virtual impedance is activated. The adaptive virtual impedance is defined as:

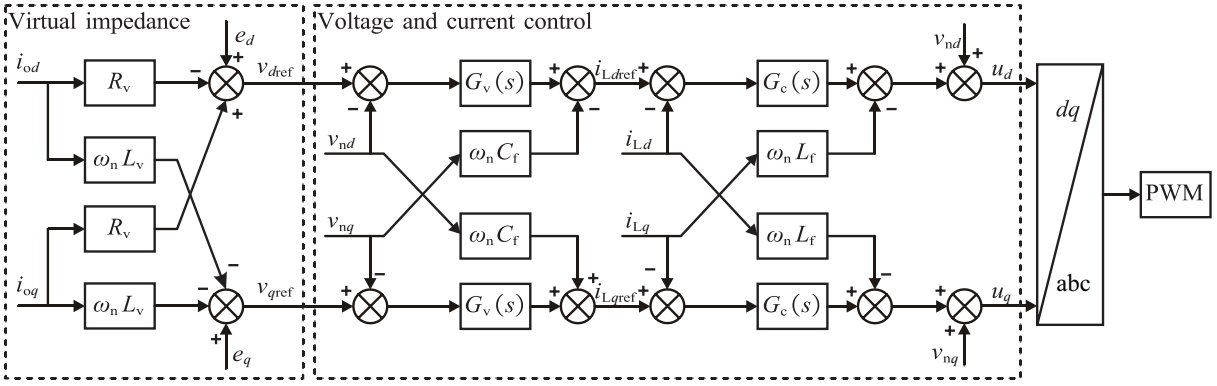

Fig. 3 Control block diagram of virtual impedance-based current limiting.

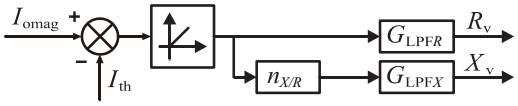

Fig. 4. Control block diagram of the adaptive virtual impedance.

$$\begin{cases} R_{\mathrm{v}} = \begin{cases} k_{\mathrm{R}}\left(I_{\mathrm{omag}} - I_{\mathrm{th}}\right), & I_{\mathrm{omag}} > I_{\mathrm{th}} \\ 0, & I_{\mathrm{omag}} < I_{\mathrm{th}} \end{cases} \\ X_{\mathrm{v}} = n_{X/R} R_{\mathrm{v}} \end{cases} \tag{4}$$

where k_{R} represents the constant proportional coefficient, and $n_{X/R}$ denotes the ratio of reactance to resistance in the virtual impedance.

To mitigate the influence of current ripple on the virtual impedance, a low-pass filter (LPF) is introduced after the virtual impedance, and the transfer function of filter is expressed as:

$$\begin{cases} G_{\mathrm{LPF}X}(s) = \dfrac{\omega_{\mathrm{LPF}X}}{s + \omega_{\mathrm{LPF}X}} \\ G_{\mathrm{LPF}R}(s) = \dfrac{\omega_{\mathrm{LPF}R}}{s + \omega_{\mathrm{LPF}R}} \end{cases} \tag{5}$$

In order to ensure that the inverter output current $I_{\mathrm{omag\_max}}$ does not exceed the rated value I_{lim} even when the grid voltage drops to zero, the magnitude of the virtual impedance can be calculated as:

$$I_{\mathrm{omag\_max}} = \frac{V_{\mathrm{n}}}{\sqrt{R_{\mathrm{v}}^2 + \left(X_{\mathrm{v}} + X_{\mathrm{c}}\right)^2}} \leqslant I_{\mathrm{lim}} \tag{6}$$

Substituting (4) into (6) yields that,

$$k_{\mathrm{R}} \geqslant k_{\mathrm{R\_min}} = \frac{-n_{X/R} X_{\mathrm{c}} + \sqrt{\left(n_{X/R}^2 + 1\right)\dfrac{V_{\mathrm{n}}^2}{I_{\mathrm{lim}}^2} - X_{\mathrm{c}}^2}}{\left(n_{X/R}^2 + 1\right)\left(I_{\mathrm{lim}} - I_{\mathrm{th}}\right)} \tag{7}$$

where $k_{\mathrm{R\_min}}$ is the minimum value of the proportional coefficient k_{R} to avoid the current exceeding the rated value.

The variation of $k_{\mathrm{R\_min}}$ with different reactance-to-resistance ratios $n_{X/R}$ is shown in Fig. 5. It can be observed that as $n_{X/R}$ increases, the range of k_{R} values expands. To achieve better suppression of the fault current, the value of k_{R} should be greater than the corresponding $k_{\mathrm{R\_min}}$ for the system's reactance-to-resistance ratio.

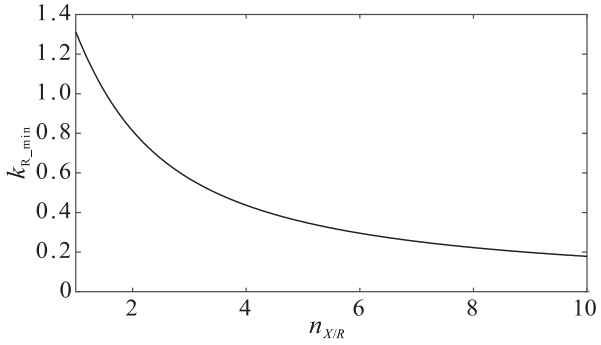

Fig. 5. The range of $k_{\mathrm{R\_min}}$ values for different reactance-to-resistance ratios $n_{\mathrm{X/R}}$.

III. Stability Analysis

Based on the adaptive virtual impedance characteristics as shown in Fig. 3, it can be observed that the adaptive virtual impedance is deactivated during normal grid voltage conditions. However, after a grid voltage drop, the adaptive virtual impedance is activated automatically to suppress the fault current. Therefore, this section investigates the stability of the grid-forming inverter with adaptive virtual impedance using the small-signal approach.

To begin with, we establish the small-signal model of the adaptive virtual impedance module by linearizing (1), (3), and (4), which yields:

$$\begin{cases} \hat{u}_{d\mathrm{ref}} = \hat{e}_d - \left[R_{\mathrm{v}0}\hat{i}_{od} + \hat{R}_{\mathrm{v}} i_{od0} - \left(X_{\mathrm{v}0}\hat{i}_{oq} + \hat{X}_{\mathrm{v}} i_{oq0}\right)\right] \\ \hat{u}_{q\mathrm{ref}} = \hat{e}_q - \left[X_{\mathrm{v}0}\hat{i}_{od} + \hat{X}_{\mathrm{v}} i_{od0} + \left(R_{\mathrm{v}0}\hat{i}_{oq} + \hat{R}_{\mathrm{v}} i_{oq0}\right)\right] \end{cases} \tag{8}$$

$$\hat{i}_{\mathrm{omag}} = \frac{i_{od0}}{i_{\mathrm{omag}0}}\hat{i}_{\mathrm{o}d} + \frac{i_{oq0}}{i_{\mathrm{omag}0}}\hat{i}_{oq} \tag{9}$$

$$\begin{cases} \hat{R}_v = k_R G_{\mathrm{LPF}R}(s)\hat{i}_{\mathrm{omag}} \\ \hat{X}_{\mathrm{v}} = n_{X/R} k_R G_{\mathrm{LPF}X}(s)\hat{i}_{\mathrm{omag}} \end{cases} \tag{10}$$

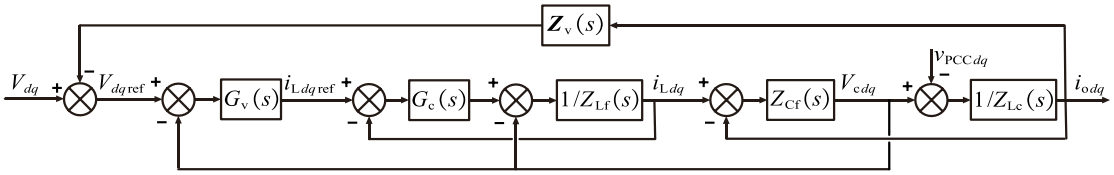

Fig. 6 Control process diagram of the system.

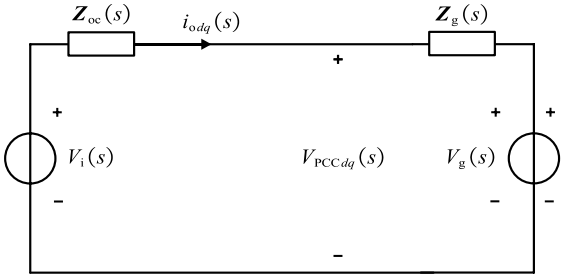

Fig. 7 Impedance model of the system.

The small-signal model for adaptive virtual impedance control can be derived by solving (8) to (10), leading to the following expression:

$$\begin{bmatrix}\hat{u}_{d\mathrm{ref}}\\ \hat{u}_{q\mathrm{ref}}\end{bmatrix}=\begin{bmatrix}\hat{e}_d\\ \hat{e}_q\end{bmatrix}-\boldsymbol{Z}_{\mathrm{v}}\begin{bmatrix}\hat{i}_{\mathrm{o}d}\\ \hat{i}_{\mathrm{o}q}\end{bmatrix} \tag{11}$$

where Z_{v} represents the virtual impedance, which is defined by the following expression:

$$\boldsymbol{Z}_{\mathrm{v}}=\begin{bmatrix}R_{\mathrm{v}0} & -X_{\mathrm{v}0}\\ X_{\mathrm{v}0} & R_{\mathrm{v}0}\end{bmatrix}+\frac{k_{\mathrm{R}}}{i_{\mathrm{omag}0}}$$
$$\begin{bmatrix}i_{od0}\left(i_{od0}G_{\mathrm{LPF}R}-n_{X/R}\,i_{oq0}G_{\mathrm{LPF}X}\right) & i_{oq0}\left(i_{od0}G_{\mathrm{LPF}R}-n_{X/R}\,i_{oq0}G_{\mathrm{LPF}X}\right)\\ i_{od0}\left(i_{oq0}G_{\mathrm{LPF}R}+n_{X/R}\,i_{od0}G_{\mathrm{LPF}X}\right) & i_{oq0}\left(i_{oq0}G_{\mathrm{LPF}R}+n_{X/R}\,i_{od0}G_{\mathrm{LPF}X}\right)\end{bmatrix} \tag{12}$$

From (12), it can be observed that $Z_{\mathrm{v}}(1,2) \neq Z_{\mathrm{v}}(2,1)$ and $Z_{\mathrm{v}}(1,1) \neq Z_{\mathrm{v}}(2,2)$, indicating that Z_{v} is an asymmetric matrix. As a result, the independent analysis of the *d*-axis and *q*-axis component is impossible, and the coupling relationship between the *d*-axis and *q*-axis needs to be considered. By combining the voltage-current control loop and the LCL filter section, a impedance model is established, as illustrated in Fig. 6.

The transfer function of the system in Fig. 6 can be derived as:

$$i_{\mathrm{o}dq}(s)=\boldsymbol{G}_{\mathrm{I}}(s)e_{dq}(s)-\boldsymbol{Y}_{\mathrm{o}}(s)V_{\mathrm{PCC}dq}(s) \tag{13}$$

Since the grid-forming inverter is controlled to exhibit a voltage-source characteristic, by manipulating (13) and considering V_{PCC} as the output variable, the resulting expression can be obtained as:

$$V_{\mathrm{PCC}dq}(s)=V_{\mathrm{i}}(s)-\boldsymbol{Z}_{\mathrm{oc}}(s)i_{\mathrm{o}dq}(s) \tag{14}$$

where V_{i} represents the open-circuit voltage of the inverter, and Z_{oc} denotes the port impedance of the inverter. The details of them are shown in (15).

$$\begin{cases}V_{\mathrm{i}}(s)=\boldsymbol{Y}_{\mathrm{o}}^{-1}(s)\boldsymbol{G}_{\mathrm{I}}(s)e_{dq}(s)\\ \boldsymbol{Z}_{\mathrm{oc}}(s)=\boldsymbol{Y}_{\mathrm{o}}^{-1}(s)\end{cases} \tag{15}$$

Based on (14), the impedance model of the inverter and grid system can be established, as shown in Fig. 7. The grid is represented by an equivalent voltage source V_{g} and line impedance Z_{g}. Therefore, the stability of the system can be determined using impedance ratio criteria [11]. In general, the line impedance is inductive, and assuming the line has an equivalent inductance L_{g}, the impedance transfer function of the line in the dq reference frame can be expressed by,

$$\boldsymbol{Z}_{\mathrm{g}}(s)=\begin{bmatrix}sL_{\mathrm{g}} & -\omega L_{\mathrm{g}}\\ \omega L_{\mathrm{g}} & sL_{\mathrm{g}}\end{bmatrix} \tag{16}$$

Based on the Kirchhoff's voltage law, the injected current can be computed by

$$i_{\mathrm{o}dq}(s)=\left[\boldsymbol{Z}_{\mathrm{oc}}(s)+\boldsymbol{Z}_{g}(s)\right]^{-1}\left[V_{\mathrm{i}}(s)-V_{\mathrm{g}}(s)\right] \tag{17}$$

By transforming (17), the following expression can be obtained:

$$i_{\mathrm{o}dq}(s)=\left[\boldsymbol{I}+\boldsymbol{Z}_{\mathrm{g}}^{-1}(s)\boldsymbol{Z}_{\mathrm{oc}}(s)\right]^{-1}\boldsymbol{Z}_{\mathrm{g}}^{-1}(s)\left[V_{\mathrm{i}}(s)-V_{\mathrm{g}}(s)\right] \tag{18}$$

where *I* represents the identity matrix.

Since $V_{\mathrm{i}}(s)$–$V_{\mathrm{g}}(s)$ and $Z_{\mathrm{g}}(s)$ in (18) are stable, the stability of the system depends on whether the first term on the right-hand side is stable. It is worth noting that $[I + Z_{\mathrm{g}}^{-1}(s)Z_{\mathrm{oc}}(s)]^{-1}$ represents the closed-loop transfer function of a negative feedback control system with a feedforward channel gain of I and a feedback channel gain of $Z_{\mathrm{g}}^{-1}(s)Z_{\mathrm{oc}}(s)$. The open-loop transfer function of this system corresponds to the system's impedance ratio function, which can be expressed as:

$$\boldsymbol{L}(s)=\boldsymbol{Z}_{\mathrm{g}}^{-1}(s)\boldsymbol{Z}_{\mathrm{oc}}(s) \tag{19}$$

The stability condition for the system is that $L(s)$ satisfies the generalized Nyquist criterion [12]. Since $Z_{\mathrm{oc}}(s)$ is derived through a combination of LPF and PI controller, it does not contain the right-half-plane poles. The line impedance $Z_{\mathrm{g}}(s)$ ensures system stability when powered by an ideal voltage source, implying that $Z_{\mathrm{g}}^{-1}(s)$ also does not have the right-half-plane poles. Therefore, the stability criterion for the system is as follows: if the characteristic root locus of $L(s)$ does not encircle the region (–1, 0) counter clockwise, then the closed-

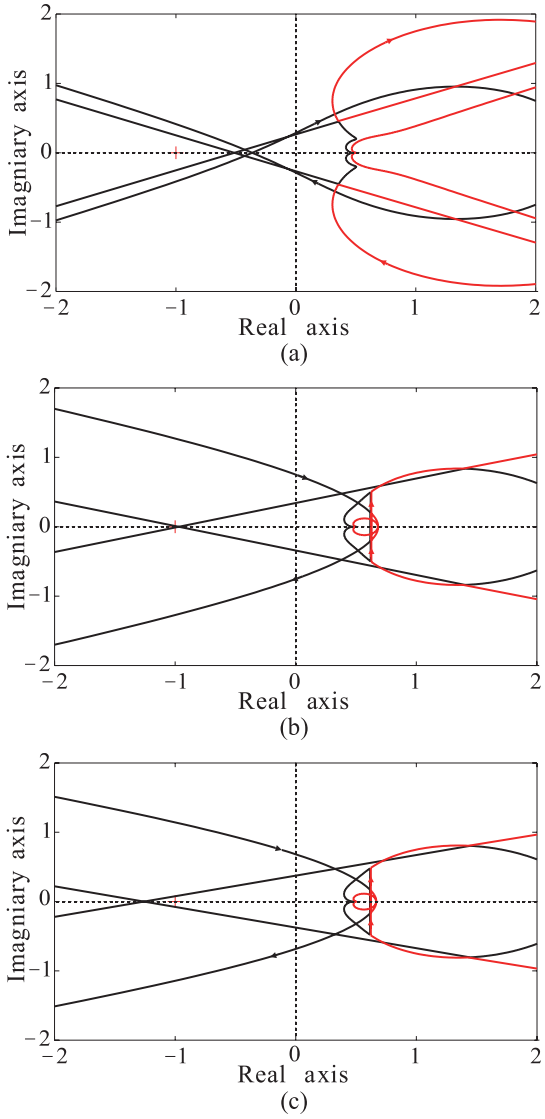

Fig. 8 Generalized Nyquist plots for varying values of ω_{LPFX}. (a) 10π, (b) 50π and (c) 200π.

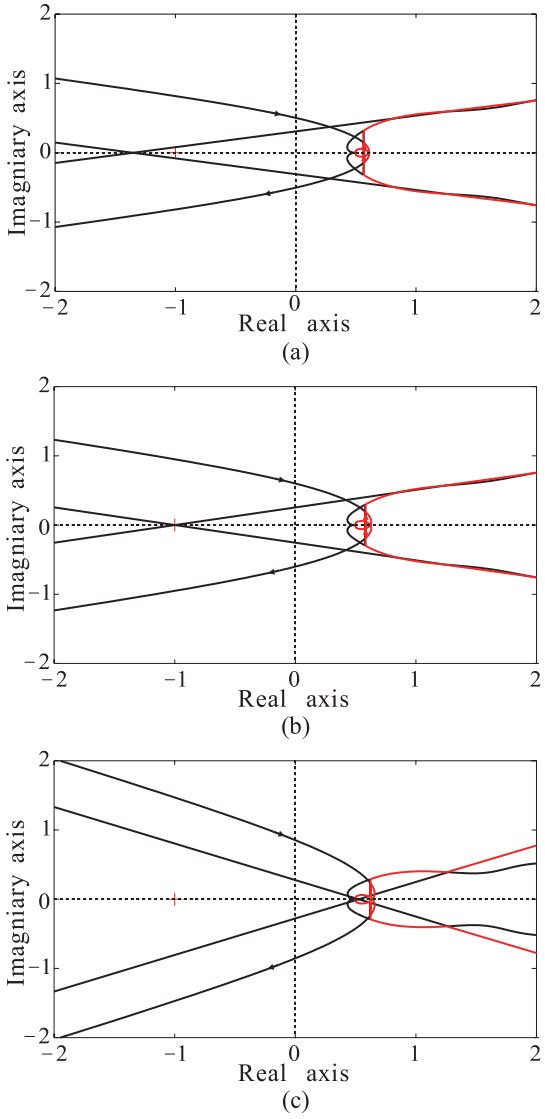

Fig. 9 Generalized Nyquist plots for varying values of ω_{LPFX}. (a) = 50π, (b) 200π and (c) 500π.

loop system is stable.

Based on this criterion, the influence of filter parameters on system stability can be analyzed. Firstly, by setting $G_{LPFR}(s) = 1$, the impact of the cutoff frequency ω_{LPFX} of the virtual inductor LPF on the system is analyzed. When ω_{LPFX} is set to 10π, 150π, and 200π respectively, the Nyquist plots of $L(s)$ are shown in Fig. 8. From Fig. 8(a)–(c), it can be observed that as ω_{LPFX} increases, the Nyquist curve gradually approaches the point (–1, 0). When $\omega_{LPFX} = 150\pi$, the Nyquist curve passes through the point (–1, 0), indicating the system is in the critically stable state. When $\omega_{LPFX} = 200\pi$, the Nyquist curve encloses the point (–1, 0), resulting in instability. Therefore, reducing the cutoff frequency ω_{LPFX} of the virtual inductor filter is beneficial for system stability. To ensure a sufficient stability margin, the cutoff frequency of the virtual inductor filter is set to $\omega_{LPFX} = 30\pi$.

The influence of the cutoff frequency ω_{LPFR} of the virtual resistor LPF on the system is depicted in Fig. 9. From Fig. 9(a)–(c), it is evident that as ω_{LPFR} increases, the Nyquist curve progressively moves away from the (–1, 0) point. For $\omega_{LPFR} = 50\pi$, the Nyquist curve encloses the (–1, 0) point, indicating the instability. However, for $\omega_{LPFR} = 200\pi$, the Nyquist curve passes through the (–1, 0) point, indicating the critical stability. When $\omega_{LPFR} = 500\pi$, the Nyquist curve does not enclose the (–1, 0) point, indicating that the system is stable. Hence, increasing the cutoff frequency ω_{LPFR} of the virtual resistor LPF can improve the system stability.

IV. Simulation Analysis

To verify the theoretical analysis of the fault current limitation capability and system stability of the adaptive virtual impedance control strategy, the electromagnetic transient model of an adaptive virtual impedance-based GFI was developed in Matlab/Simulink. The simulation model enabled the analysis and verification of the control strategy's performance under different fault conditions. The system parameters are showed in Table I.

TABLE I
SYSTEM PARAMETERS OF THE CONVERTER

Symbol	Quantity	Values
V_{dc}	DC voltage	1000 V
U_g	Grid voltage	311 V
L_f	Inverter side inductance of filter	3.5 mH
R_f	Parasitic resistance of L_f	0.1 Ω
C_f	Capacitance of filter	50 μF
L_c	Grid side inductance of filter	5 mH
R_c	Parasitic resistance of L_c	0.05 Ω
L_g	Grid impedance	10 mH
P_0	Reference active power	4 kW
Q_0	Reference reactive power	0 kVar
f_0	Grid frequency	50 Hz
V_{ref}	Reference voltage magnitude	311 V
J	Inertia value	159.15 kg·m^2
D_p	Damping coefficient	2000
k_{pv}	Proportional coefficient of voltage controller	0.2859
k_{iv}	Integral coefficient of voltage controller	594.85
k_{pc}	Proportional coefficient of current controller	54.978
k_{ic}	Integral coefficient of current controller	1570.8
k_R	Coefficient of virtual impedance	1

A. Stability Verification of GFIs With Adaptive Virtual Impedance

The simulation waveforms in Figs. 10 and 11 illustrate the impact of the cutoff frequencies, ω_{LPFX} and ω_{LPFR}, of the virtual reactance and virtual resistance filters on the stability of the GFI system. After the grid voltage drops from 1.0 to 0.6 p.u. at t = 5 s, the GFI system reaches a steady state. At t = 20 s, the cutoff frequencies of the filters are increased 15 and 20 times, respectively.

In Fig. 10(a), the cutoff frequency ω_{LPFX} of the virtual reactance is fixed at 10π. In Fig. 10(b) and (c), the cutoff frequency ω_{LPFX} of the virtual reactance is increased to 150π and 200π, respectively, at t = 20 s. When ω_{LPFX} is 10π, the GFI maintains a stable PCC voltage magnitude of 168 V, as shown in Fig.10(a). However, when ω_{LPFX} is increased to 150π, the voltage magnitude starts oscillation within a certain range, indicating system instability, as depicted in Fig. 10(b). Similarly, when ω_{LPFX} is increased to 200π, the voltage magnitude exhibits irregular oscillations with a larger amplitude, indicating the system instability, as shown in Fig. 10(c). The simulation analysis results align with the theoretical analysis presented in Fig. 8, demonstrating that reducing ω_{LPFX} enhances the stability of the GFI system with the adaptive virtual impedance.

In Fig.11(a), the cutoff frequency ω_{LPFR} of the virtual resistance filter is maintained at a constant value of 500π, while in Fig. 11(b) and (c), ω_{LPFR} is decreased to 200π and 50π at t = 20 s. From Fig. 11(a), it can be observed that when ω_{LPFR} is constant at 500π, the GFI maintains a stable PCC voltage magnitude of 168 V. However, when ω_{LPFR} is decreased to 200π, the voltage magnitude starts oscillating within a certain range, indicating the system instability, as shown in Fig. 11(b). Furthermore, when ω_{LPFR} is further decreased to 50π, the voltage magnitude exhibits the irregular oscillations with an increasing amplitude,

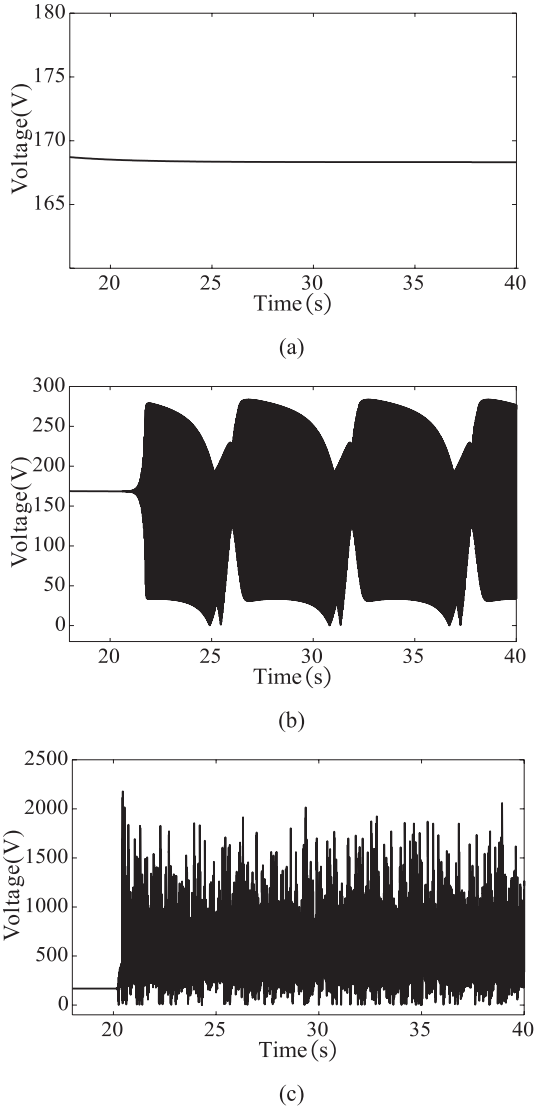

Fig. 10 Impacts of the bandwidth ω_{LPFX} of virtual reactance filter on stability. (a) ω_{LPFX} = 10π. (b)Step-wise increase from 10π to 150π. (c) Step-wise increase from 10π to 200π.

indicating the system instability, as depicted in Fig. 11(c). The simulation analysis results align with the theoretical analysis in Fig. 9, which suggests that increasing ω_{LPFR} can improve system stability. Therefore, in practical applications, the use of a LPF with virtual resistance should be avoided.

B. Comparison of the Fault Current Limitation Capability

A simulation analysis was performed to evaluate the performance of three control methods: without virtual impedance, constant virtual impedance, and adaptive virtual impedance. The simulation scenario involved a three-phase voltage drop in the grid from 1.0. to 0.85 p.u. at 5 s. In the analysis, the constant virtual impedance was set to R_v = 0.41 Ω and $X_v = 5R_v$, which are equivalent to the steady-state values of the adaptive virtual impedance. The simulation results are presented in Fig. 12.

From Fig. 12(a), it can be observed that without the virtual

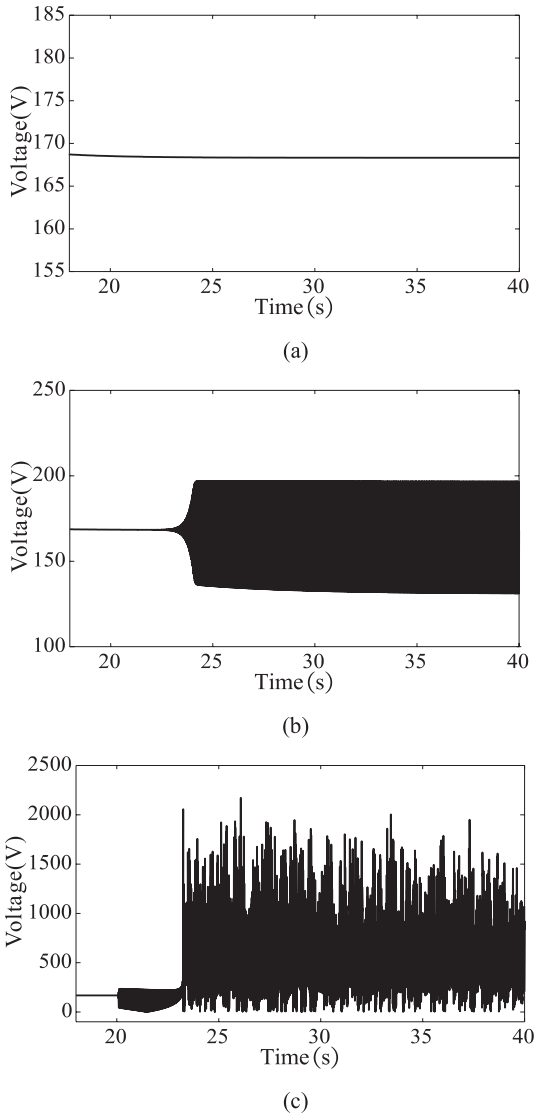

Fig. 11 Impacts of the bandwidth ω_{LPFR} of virtual reactance filter on stability. (a) ω_{LPFR} = 500π. (b) Step-wise decrease from 500π to 200π. (c) Step-wise decrease from 500π to 50π.

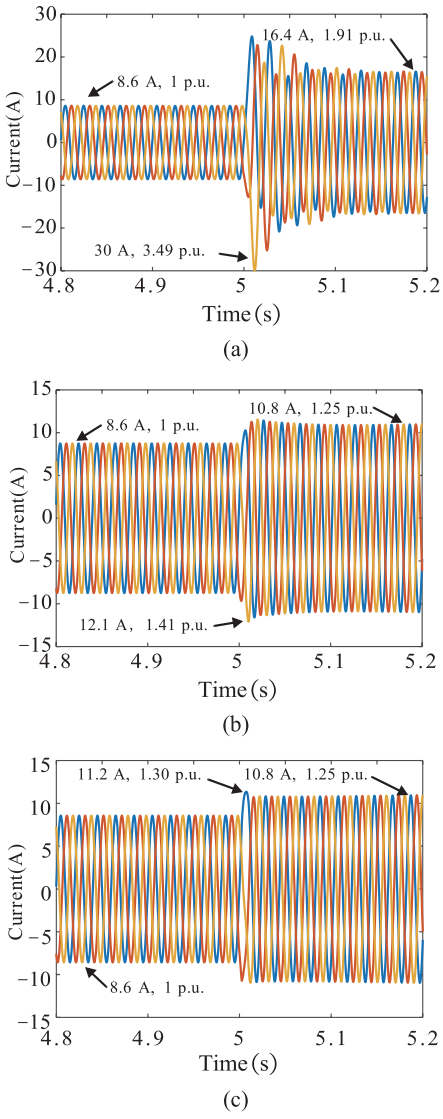

Fig. 12 Current waveforms during three-phase voltage drop from 1.0 to 0.85 p.u.. (a) Without virtual impedance. (b) With constant. (c) Adaptive virtual impedance.

impedance control strategy, the peak value of the transient current is 3.49 p.u., and the current exhibits oscillations, which lasting for 0.52 s. For the constant virtual impedance control strategy, the peak value of the transient current is 1.41 p.u., and the transient period is 0.18 s, as shown in Fig. 12(b). With the adaptive virtual impedance control strategy, the peak value of transient current is 1.30 p.u., and transient period is 0.03 s during the fault.

In comparison of three control strategies, the peak value of the transient current of adaptive virtual impedance during grid fault is 92.2% of that without virtual impedance, and 37.2% of the constant virtual impedance approach. The transient periods of the adaptive virtual impedance is 5.8% and 16.7% of that without virtual impedance and constant virtual impedance approach, respectively. Hence, the adaptive virtual impedance control strategy can effectively suppress the fault current and improve the transient performances.

A simulation analysis was conducted with the condition of a voltage drop in the grid from 1.0 to 0.7 p.u. at 5 s. The simulation results are depicted in Fig. 13.

From Fig. 13, it can be observed that due to the greater drop depth in the grid voltage, the peak value of the fault currents with the three control strategies are increased as compared to that in Fig. 12. Without virtual impedance, the peak fault current is 6.62 p.u.. With the constant virtual impedance, the maximum fault current is 2.13 p.u.. With the adaptive virtual impedance, the peak value of transient current is reduced to 1.47 p.u..

Compared to Fig. 12(b), the peak value of the transient current in Fig. 13(b) is increased about 1.51 times (from 1.41 to 2.13 p.u.). Hence, the constant virtual impedance can suppress the fault current, but this suppression capability is invariable. When the grid fault worsens, it may cause overcurrent and trigger protective actions of the GFIs. On the other hand, the adaptive virtual impedance can retain the peak fault current almost

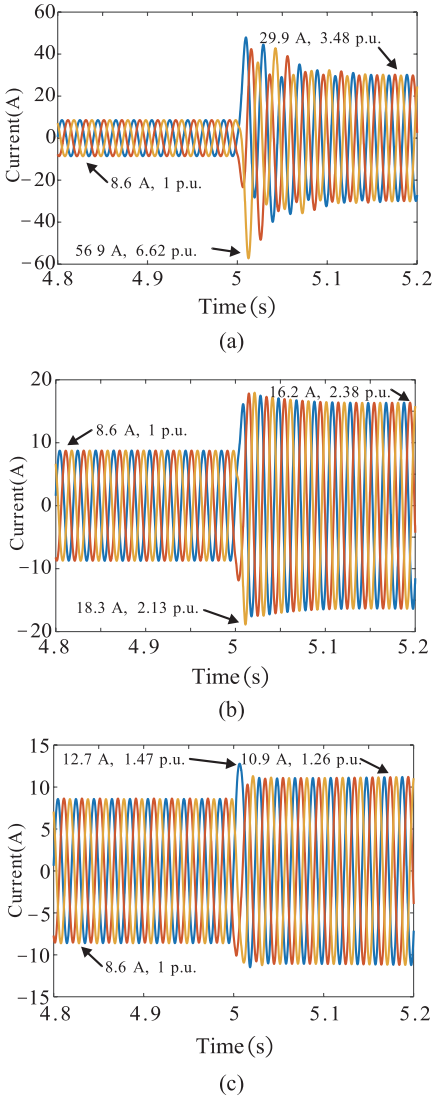

Fig. 13 Current waveform during three-phase voltage drop from 1.0 p.u. to 0.7 p.u.. (a) Without virtual impedance. (b) With constant. (c) Adaptive virtual impedance.

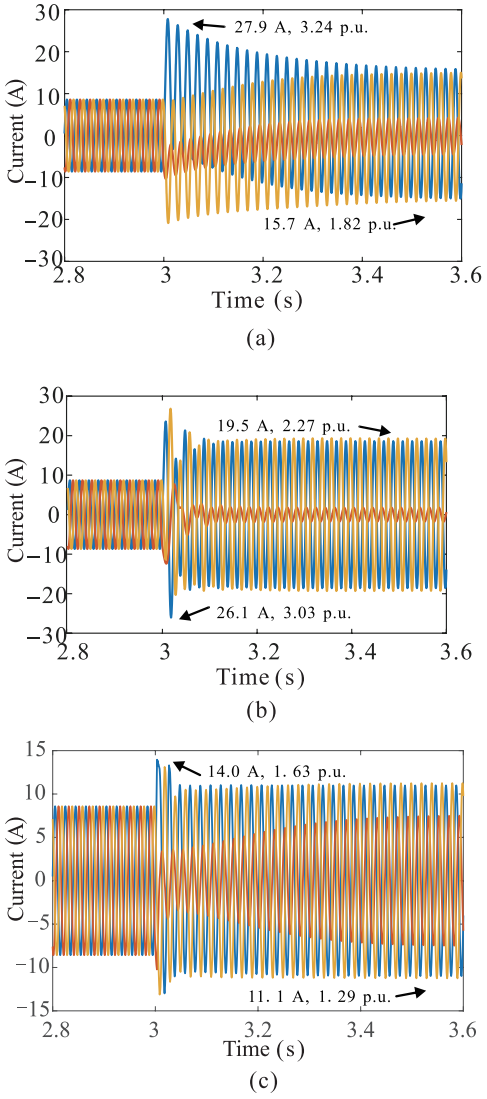

Fig. 14 Current waveform during single-phase voltage drop from 1.0 p.u. to 0.7 p.u.. (a) Without virtual impedance. (b) With constant. (c) Adaptive virtual impedance.

constant (1.3 and 1.47 p.u.) under different voltage drop depth.

The simulation results of single-phase voltage drop is shown in Fig. 14. From Fig. 14, it can be observed that without the virtual impedance control strategy, the peak value of the transient current is 3.24 p.u. For the constant virtual impedance control strategy, the peak value of the transient current is 3.03 p.u.. With the adaptive virtual impedance control strategy, the peak value of transient current is 1.63 p.u.. However, the control method is a little different with Fig. 13. To limit the unbalanced three-phase current, three single-phase adaptive virtual impedance are used, where the virtual impedance is proportional to the current magnitude of each phase.

V. Real-Time Platform-Based Valuation

A. Case Study of Infinite Bus System

To further verify the simulation results, the experiments are carried out based on the RT-LAB platform. The grid voltage is set to drop to 0.85 p.u. at t = 5 s. The experiments results are presented in Fig. 15. It can be observed that without the virtual impedance control strategy, the peak value of the transient current is 3.98 p.u.. For the constant virtual impedance control strategy, the peak value of the transient current is 1.64 p.u.. With the adaptive virtual impedance control strategy, the peak value of the transient current is 1.34 p.u..

In comparison of the three control strategies, the peak value of the transient current of adaptive virtual impedance during grid fault is 33.7% of that without virtual impedance, and 81.7% of the constant virtual impedance approach.

The experimental waveforms of the current when the voltage drops from 1.0 to 0.7 p.u. are shown in Fig. 16, from which it can be observed that without the virtual impedance control strategy, the peak value of the transient current is 7.67 p.u.. For the constant virtual impedance control strategy, the peak value of the transient current is 4.51 p.u.. With the adaptive virtual

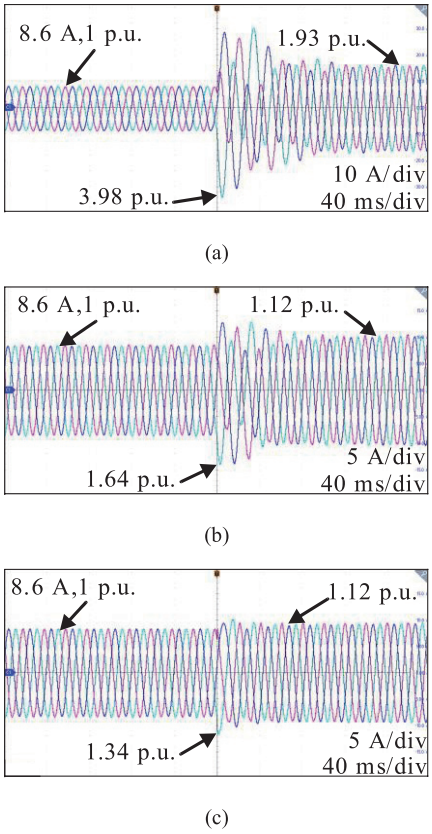

Fig. 15 Experimental waveform of current during the voltage drop from 1.0 to 0.85 p.u.. (a) Without virtual impedance. (b) With constant. (c) Adaptive virtual impedance.

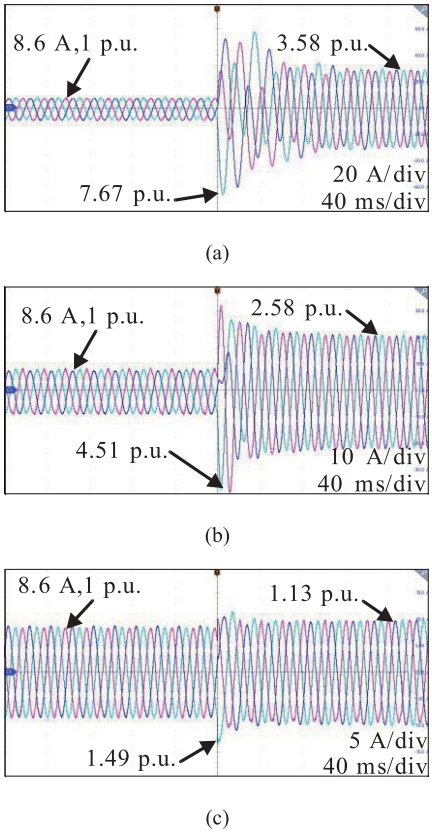

Fig. 16 Experimental waveform of current during the voltage drop from 1.0 to 0.7 p.u.. (a) Without virtual impedance. (b) With constant. (c) Adaptive virtual impedance.

impedance control strategy, the peak value of the transient current is 1.49 p.u..

In comparison of three control strategies, the peak value of the transient current of adaptive virtual impedance during grid fault is 19.4% of that without virtual impedance, and 33% of the constant virtual impedance approach.

B. Case Study of IEEE 9-Bus System

To verify the effectiveness of the proposed control strategy in suppressing fault currents, this paper establishes an experimental platform based on a test system 9-bus provided by IEEE in OPAL-RT. The system schematic diagram is shown in Fig. 17. In this diagram, the synchronous generator G1 is connected to bus 1 with a capacity of 65 MW. Bus 2 is connected to synchronous generator G2 and a GFI with capacities of 44.8 MW and 2 MW, the synchronous generator G3 is connected to bus 3 with a capacity of 60 MW. The equivalent lengths of lines 7, 8, and 9 are 150 km. The parameters of the GFI are showed in Table II.

A three-phase to ground short-circuit fault occurs at bus 5 at t = 15 s, and cleared at t = 15.2 s. The current waveforms during the fault are shown in Fig. 18. It can be observed that without the virtual impedance control strategy, the peak value of the transient current is 1.9 p.u. during grid fault, and the steady-state value of the fault current is 1.44 p.u.. For the constant virtual impedance control strategy, the peak value of the transient current is 1.83 p.u., and the steady-state value of the fault current is 1.3 p.u..

With the adaptive virtual impedance control strategy, the peak value of the transient current is 1.13 p.u., and the steady-state value of the fault current is 1.11 p.u.. In comparison of three control strategies, with constant virtual impedance approach the peak value of transient current is reduced to 61.7%. While with the adaptive virtual impedance, the peak value of the transient current is further reduced to 59.5%. Hence, the approach of adaptive virtual impedance can limit the transient current effectively as compared to the constant virtual impedance approach. Therefore, the adaptive virtual impedance exhibits a significant suppression effect on the fault current of the inverter, during the transient and steady state of the fault.

VI. Conclusions

This paper addresses the issue of overcurrent in grid-forming inverters under grid voltage faults by the proposed adaptive virtual impedance control strategy. The strategy dynamically adjusts the virtual impedance based on the magnitude of the current. Compared to traditional virtual impedance control strategies, this method demonstrates good current limiting

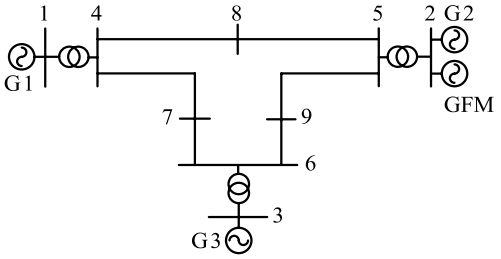

Fig. 17 Architecture diagram of IEEE 9-bus system with GFI.

TABLE II
GFI PARAMETERS

Symbol	Quantity	Values
V_{dc}	DC voltage	1200 V
L_f	Inductance of filter	0.3 mH
R_f	Parasitic resistance of L_f	0.001 Ω
C_f	Capacitance of filter	40 μF
P_0	Reference active power	2 kW
f_0	Grid frequency	50 Hz
J	Inertia value	25 kg·m^2
D_p	Damping coefficient	1350
k_R	Coefficient of virtual impedance	10

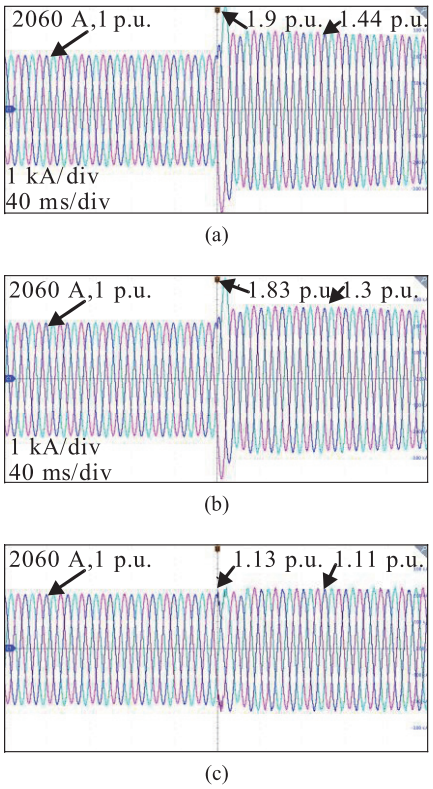

Fig. 18 Experimental waveforms of IEEE 9-bus system. (a) Without virtual impedance. (b) With constant. (c) Adaptive virtual impedance.

performance under different voltage drop depths. When the voltage drops from 1.0 to 0.6 p.u. and 0.3 p.u., the adaptive virtual impedance strategy reduces the fault current transient values by 24.5% and 52.6%, respectively, compared to the constant virtual impedance control strategy and without virtual impedance approach. The stability of the adaptive virtual impedance control system is analyzed based on the derived impedance model. The results indicate that reducing the cut-off frequency of LPF in the virtual inductance loop contributes to improve system stability. Moreover, increasing the cut-off frequency of the LPF in the virtual resistance loop enhances system stability.

REFERENCES

[1] Y. Gu and T. C. Green, "Power system stability with a high penetration of inverter-based resources," in *Proceedings of the IEEE*, vol. 111, no. 7, pp. 832–853, Sept. 2023.

[2] L. Xiong, X. Liu, Y. Liu, and F. Zhuo, "Modeling and stability issues of voltage-source converter-dominated power systems: A review," in *CSEE Journal of Power and Energy Systems*, vol. 8, no. 6, pp. 1530–1549, Nov. 2020.

[3] R. Rosso, X. Wang, M. Liserre, X. Lu, and S. Engelken, "Grid-forming converters: Control approaches, grid-synchronization, and future trends—A review," in *IEEE Open Journal of Industry Applications*, vol. 2, pp. 93–109, Apr. 2021.

[4] B. Fan, T. Liu, F. Zhao, H. Wu, and X. Wang, "A review of current-limiting control of grid-forming inverters under symmetrical disturbances," in *IEEE Open Journal of Power Electronics*, vol. 3, pp. 955–969, Dec. 2022.

[5] B. Fan and X. Wang, "Equivalent circuit model of grid-forming converters with circular current limiter for transient stability analysis," in *IEEE Transactions on Power Systems*, vol. 37, no. 4, pp. 3141–3144, Jul. 2022.

[6] L. Zhou, "Harmonic current and inrush fault current coordinated suppression method for VSG under non-ideal grid condition," in *IEEE Transactions on Power Electronics*, vol. 36, no. 1, pp. 1030–1042, Jan. 2021.

[7] T. Liu, X. Wang, F. Liu, K. Xin, and Y. Liu, "A current limiting method for single-loop voltage-magnitude controlled grid-forming converters during symmetrical faults," in *IEEE Transactions on Power Electronics*, vol. 37, no. 4, pp. 4751–4763, Apr. 2022.

[8] B. Fan and X. Wang, "Fault recovery analysis of grid-forming inverters with priority-Based current limiters," in *IEEE Transactions on Power Systems*, vol. 38, no. 6, pp. 5102–5112, Nov. 2023.

[9] J. Erdocia, A. Urtasun, and L. Marroyo, "Dual voltage–current control to provide grid-forming inverters with current limiting capability," in *IEEE Journal of Emerging and Selected Topics in Power Electronics*, vol. 10, no. 4, pp. 3950–3962, Aug. 2022.

[10] H. Wu and X. Wang, "Small-signal modeling and controller parameters tuning of grid-forming VSCs with adaptive virtual impedance-based current limitation," in *IEEE Transactions on Power Electronics*, vol. 37, no. 6, pp. 7185–7199, Jun. 2022.

[11] J. Sun, "Impedance-based stability criterion for grid-connected inverters," in *IEEE Transactions on Power Electronics*, vol. 26, no. 11, pp. 3075–3078, Nov. 2011.

[12] B. Wen, D. Boroyevich, R. Burgos, P. Mattavelli, and Z. Shen, "Inverse Nyquist stability criterion for grid-tied inverters," in *IEEE Transactions on Power Electronics*, vol. 32, no. 2, pp. 1548–1556, Feb. 2017.

Fengshun Jiao received his B.E. degree in electrical engineering and automation from Huazhong University of Science and Technology, Wuhan, China, in 2008, and the Ph.D. degree in power systems and automation from Huazhong University of Science and Technology, Wuhan, China, in 2013. He is affiliated with the Shenzhen Power Supply Bureau of China Southern Power Grid. He is primarily engaged in the planning and research of novel power systems.

Jie Zhang received his B.E. degree in electrical engineering and automation from Tsinghua University, Beijing, China, in 2007, and the M.S. degree in electrical engineering from Tsinghua University, Beijing, China, in 2018. He is affiliated with the Shenzhen Power Supply Bureau of China Southern Power Grid, where he specializes in research on power grid planning.

Xinming Jiang received his Bachelor's degree in electrical engineering and automation from North China Electric Power University, Beijing, China, in 2015, the M.S. degree in energy technology policy from Stony Brook University, New York, America, in 2016. He is affiliated with the Shenzhen Power Supply Bureau of China Southern Power Grid, where he specializes in research on power grid planning.

Xinyue Li received the B.E. degree in electrical engineering from Harbin Institute of Technology, Shenzhen, China in 2022, where he is currently working toward the M.S. degree in electrical engineering. His research interest includes the modelling and stability analysis of the grid-connected VSC.

Yunyan Yang received his B.E. degree in electrical engineering and automation from Wuhan University, Wuhan, China, in 2010, and received his M.S. degree in power aystem and automation engineering from Wuhan University, Wuhan, China, in 2012. He is affiliated with the Shenzhen Power Supply Bureau of China Southern Power Grid, where he specializes in power system relay protection.

Tao Xie received the B.E. degree in electrical engineering and automation from Wuhan University, Wuhan, China, in 2022. He is affiliated with the Shenzhen Power Supply Bureau of China Southern Power Grid, where he specializes in research on power grid planning.